ACS Catalysis

Research Article

Cite This: ACS Catal. 2018, 8, 11302−11313

pubs.acs.org/acscatalysis

Revealing the Role of Phase Structures of Bimetallic Nanocatalysts in the Oxygen Reduction Reaction

Zhi-Peng Wu,[†,‡] Shiyao Shan,[‡] Zhi-Hui Xie,[‡,#] Ning Kang,[‡] Keonwoo Park,[‡] Emma Hopkins,[‡] Shan Yan,[‡] Anju Sharma,[‡] Jin Luo,[‡] Jie Wang,[§] Valeri Petkov,*[,∥] Lichang Wang,*[,†,⊥] and Chuan-Jian Zhong*[,‡]

[†]Key Laboratory of Ministry of Education for Green Chemical Technology, R&D Center for Petrochemical Technology, and Collaborative Innovation Center of Chemical Science and Engineering, Tianjin University, Tianjin 300072, China

[‡]Department of Chemistry, State University of New York at Binghamton, Binghamton, New York 13902, United States

[§]Nanoscience and Technology Division, Argonne National Laboratory, Lemont, Illinois 60439, United States

[∥]Department of Physics, Central Michigan University, Mt. Pleasant, Michigan 48859, United States

[⊥]Department of Chemistry and Biochemistry and the Materials Technology Center, Southern Illinois University, Carbondale, Illinois 62901, United States

Supporting Information

ABSTRACT: The ability to tune the atomic-level structure of alloy nanoparticles (NPs) is essential for the design and preparation of active and stable catalysts for fuel cell reactions such as the oxygen reduction reaction (ORR), which is highly sensitive to the structure of the catalysts. We report here structurally tunable PdCu nanoparticle catalysts for the ORR obtained by varying the thermochemical treatment conditions. The phase type and the atomic structure of the nanoalloy catalysts strongly depend on the thermochemical treatment temperature and atmosphere, especially at low temperatures. While PdCu nanoalloys feature both body-centered cubic (bcc) and face-centered cubic (fcc) phase structures, a pure fcc structure, prepared at an unusually low thermochemical treatment temperature, showed the highest catalytic activity for the ORR. This was evidenced by a mass activity 8 times higher than that of commercial Pd catalyst. This activity enhancement was shown to be linked to the nanostructural tuning between fcc and bcc structures, as supported by systematic characterization using X-ray diffraction (XRD) coupled with pair distribution function (PDF) analysis. The impact of phase structure on the catalytic properties of the nanocatalyst is further substantiated by computational modeling based on density functional theory (DFT). These findings provide a fresh insight into the nanostructure−activity correlation at the atomic scale, which has significant implications for the design, synthesis, and processing of highly active nanoalloy catalysts.

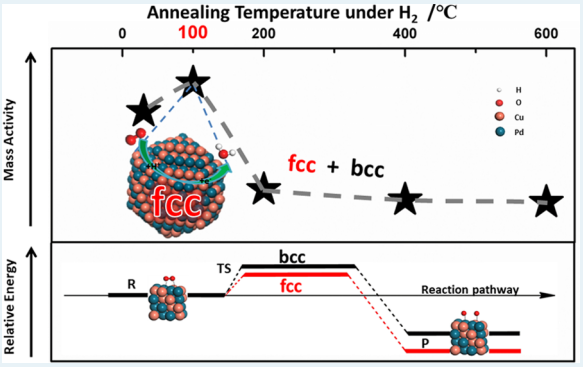

KEYWORDS: *nanocrystal structure, bimetallic nanocatalysts, palladium−copper alloy, oxygen reduction reaction, and fuel cells*

1. INTRODUCTION

Fuel cells represent an important vector of a sustainable, clean, and efficient energy source in applications ranging from portable electronic devices to automobiles. However, the practical applications are impeded largely by a lack of active and economic cathode catalysts.[1−3] A considerable amount of research effort has been dedicated to Pt- and Pt-based alloy catalysts, since they have higher catalytic activities than other catalysts for the oxygen reduction reaction (ORR) at the cathode.[4−13] However, there is a rising interest in developing Pd-based catalysts largely because they have been shown to exhibit comparable or higher catalytic activities than Pt catalysts for ORR. This finding provides a new way to cut down the high cost of cathode catalysts for fuel cells.[14−20] Alloying Pd with Cu can further help to improve the catalytic performance, since PdCu nanoalloys exhibit a strong synergistic effect. This constitutes the motivation for exploring PdCu nanocatalysts.[16,18,19,21,22] The composition−activity correlation of PdCu nanocatalysts for the ORR had been investigated by several studies. A maximum of mass activity for the ORR was obtained for the $Pd_{50}Cu_{50}$/C nanocatalyst based on different compositions in our previous work.[18] The lowest barrier energy of O_2 bond breaking and the weakest adsorption energies of O_2, O, OH, and OOH were obtained at the Pd/Cu ratio of 50:50, where the highest ORR activity was achieved.[23] It is commonly believed that a PdCu nanocatalyst with a molar

Received: August 6, 2018
Revised: October 17, 2018
Published: November 2, 2018

Downloaded via CENTRAL MICHIGAN UNIV on December 20, 2018 at 22:22:56 (UTC).
See https://pubs.acs.org/sharingguidelines for options on how to legitimately share published articles.

© 2018 American Chemical Society

DOI: 10.1021/acscatal.8b03106
ACS Catal. 2018, 8, 11302−11313

ratio of 1:1 shows the highest catalytic activity for the ORR.[14,24,25] The activity of transition metals strongly depends on the valence electronic structure, especially for the d-band center, which has been theoretically examined by Nørskov and co-workers in terms of the so-called volcano-type plot.[26−28] This model predicts that only a certain d-band center for surface Pt atoms favors a high ORR catalytic activity. The d-band center of PdCu alloys as a function of composition were calculated by Henkelman and co-workers,[25] showing that the addition of Cu lowers the d-band center of Pd, whereas the addition of Pd raises the d-band center of Cu. According to the d-band center theory, PdCu alloys may improve the ORR activity with respect to pure Pd, as supported by our previous experimental work.[18]

However, understanding how the catalytic activity is influenced by the phase structure of PdCu nanoparticles (NPs) remains elusive. The atomic-level structure of the nanocatalyst is highly sensitive to the thermal treatment conditions.[8,22,29−31] Kariuki et al.[24] showed that a mixture of face-centered cubic (fcc) and body-centered cubic (bcc) nanophases of a PdCu/C catalyst was obtained after thermal treatment at 500 °C in H_2 atmosphere, which revealed the best catalytic activity for the ORR. Wang et al.[14] demonstrated that PdCu nanocatalysts with Pd:Cu molar ratios of 1:3 and 1:1 treated at 600 °C in H_2 exhibited the highest ORR activities. Shan et al.[32] revealed that PdCu/C catalysts treated at relatively low treatment temperature (200 °C) in H_2 with an fcc structure showed the best catalytic activity for CO oxidation. PdCu/C catalysts treated at higher temperature (600 °C) in H_2 showed the coexistence of fcc and bcc structures, leading to a decrease in activity. The effect of thermal treatment on the ORR activity was also observed for the ternary catalysts.[30] In particular, PdCuM NPs (M = none, Co, or Ni)[19] showed a change from a disordered fcc structure to an ordered bcc structure after annealing at 375 °C in H_2 atmosphere and a better catalytic performance for the ORR and the ethanol oxidation reaction (EOR) in NaOH solution. Those phenomena were attributed to the ligand effect and the compressive strain on the Pd surface. In comparison with a PdCu random alloy, superior activity for the ORR was obtained by ordered PdCu NPs in 0.1 M $HClO_4$ solution.[33] Sha et al.[34] calculated the structural preference of PdCu as a function of the crystal structure using DFT and revealed that the layered $L1_1$ surface structure (fcc) exhibited significant enhancement of ORR kinetics compared to that of pure Pd. These experimental and theoretical studies arrived often at contradictory conclusions in terms of the correlation between the ORR activity and the nanophase type structure (fcc vs bcc).

Despite the extensive studies, the question of whether fcc- or bcc-structured nanocatalysts have better catalytic activity for the ORR remains unresolved. We report here new findings by studying a nanocrystal phase structure tunable PdCu (1:1) catalyst through varying the calcination temperatures in a H_2 atmosphere and its correlation with the electrocatalytic activity for the ORR. Density functional theory (DFT) calculations for PdCu catalysts with two types of crystal structures were also performed using a periodical surface model, which is superior to cluster models in this case for >5 nm particle size. Studies of the close-packed (111) surface for the fcc structure, (110) surface for the bcc structure, and open-packed (100) surfaces for both fcc and bcc structures were conducted on the elementary step of the O_2 molecule cleavage reaction to explain the experimental phenomenon at an atomic scale. While the cleavage of molecular oxygen may not be the rate-determining step of the ORR, an understanding of the reaction energetics and OH species is important for assessing the correlation of the activity with the catalyst's phase structures. The structure of the PdCu (1:1) catalyst was further characterized by high-energy X-ray diffraction (HE-XRD) coupled to atomic pair distribution functions (PDFs). While X-ray absorption fine structure (XAFS) techniques have been utilized in our previous studies to analyze the first-neighbor atomic coordination structures,[35] HE-XRD/PDFs analysis was demonstrated to be a powerful tool for analyzing the phase type of the atomic level structure of metallic NPs, which is particularly important for studying the phase structure change under different calcination temperatures. We demonstrate for the first time that the nanocatalyst's structure can be maneuvered between a pure fcc type and a mixture of fcc/bcc type structures simply by adjusting the thermal treatment temperatures (Scheme 1), and the nanocatalyst with a pure fcc structure prepared by an unusually low thermochemical treatment temperature (100 °C) exhibits higher ORR activity than that with a mixture of fcc and bcc structures.

Scheme 1. An Illustration of the Possible Phase Evolution of PdCu Nanocrystal in Terms of Fcc and Bcc Structures That Affect the Catalytic Activity for the Oxygen Reduction Reaction

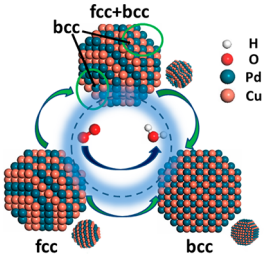

2. MATERIALS AND METHODS

Chemicals. Palladium(II) acetylacetonate [$Pd(acac)_2$, 99%], copper(II) acetylacetonate [$Cu(acac)_2$, 98%], 1,2-hexadecanediol (90%), oleic acid (99%), oleylamine (70%), benzyl ether (99%), and Nafion (5 wt %) were purchased from Aldrich. Ethanol, hexane, 2-propanol, perchloric acid, and potassium chloride were purchased from Fisher Scientific. Commercial unreduced Pd catalyst (20 wt % metal loading on activated carbon) was purchased from Strem Chemicals. Vulcan carbon XC-72 was purchased from Cabot. Millipore Milli-Q water (18.2 MΩ) was used. All gases, such as N_2, H_2, and O_2, were obtained from Airgas. Note that all chemicals were used as received.

PdCu Nanoparticle Synthesis. PdCu NPs were synthesized following a protocol reported previously.[18,36] In brief, 1 mmol of palladium(II) acetylacetonate and 1 mmol of copper(II) acetylacetonate were mixed into 150 mL of benzyl ether solvent with constant stirring and purging with N_2. Then, a controlled amount of oleic acid (5 mmol) and oleylamine (5 mmol) as the capping agents and 1,2-hexadecanediol (3 mmol) as the reducing agent were added to the solution with continuous N_2 purging. The solution was heated to 105 °C, at which N_2 purging was stopped. Afterward, the solution was heated to 220 °C, during which period the color of the

DOI: 10.1021/acscatal.8b03106
ACS Catal. 2018, 8, 11302−11313

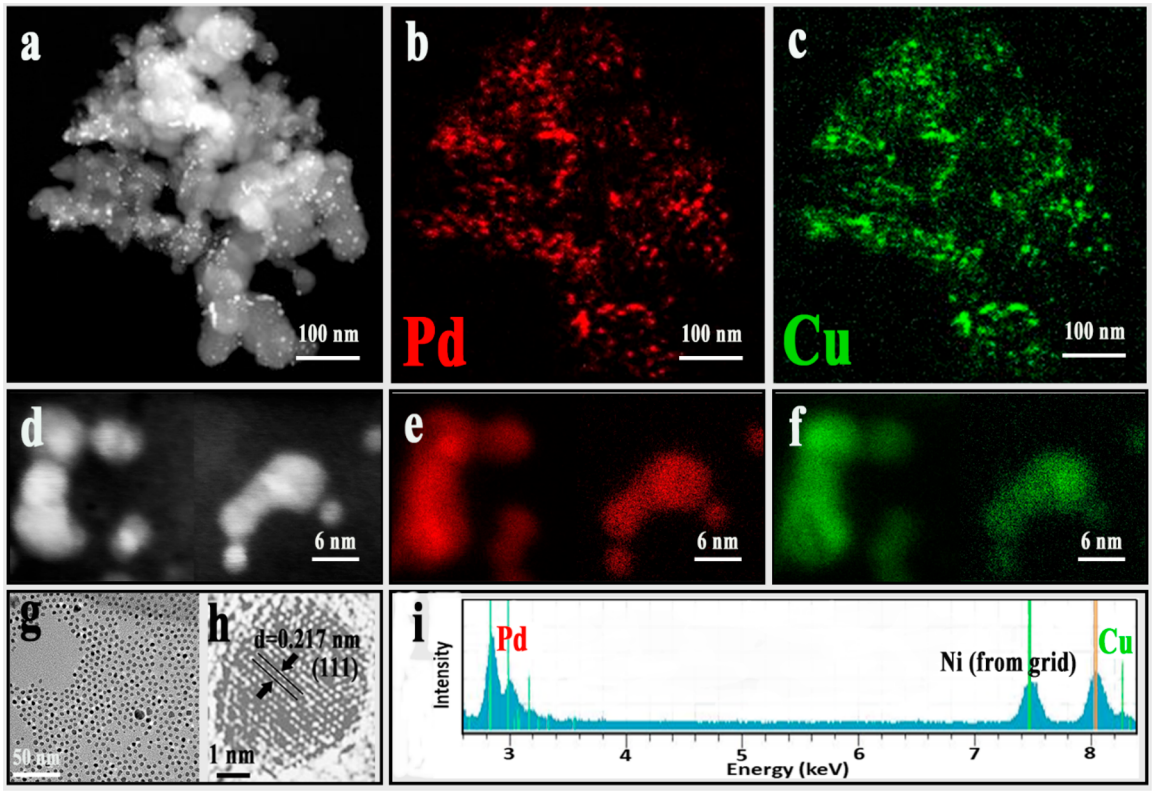

Figure 1. A representative set of HAADF-STEM images of PdCu/C (H_2/100 °C) catalyst (a) with the corresponding elemental maps (b) for Pd, (c) for Cu and a closeup view of HAADF-STEM images of PdCu/C (H_2/100 °C) catalyst (d) with corresponding elemental maps (e) for Pd and (f) for Cu. (g) A representative TEM image and (h) HRTEM image for as-synthesized PdCu NPs. (i) A STEM-EDS spectrum of PdCu/C (H_2/100 °C) catalyst.

solution turned from dark green to light brown and finally completely dark at about 150 °C, which demonstrated the formation of NPs. The solution was further refluxed at 220 °C for 30 min with stirring and then cooled down to room temperature. An amount of 300 mL ethanol was added to the final solution to wash the organic solvent, followed by centrifuging (3000 rpm) to precipitate the NPs. The resulting PdCu NPs were dispersed in hexane.

Catalyst Preparation. The assembly of NPs on the support was conducted by mixing a controlled amount of PdCu NPs and carbon support (XC-72) in hexane, followed by sonicating for 30 min and stirring overnight. The resulting carbon-supported PdCu NPs (PdCu/C) were dried under N_2. The activation of PdCu/C was implemented by a modified thermochemical process reported previously.[18] Briefly, PdCu/C was first treated at 120 °C under pure N_2 for 10 min to remove the remaining low boiling point organics. This process prevented the catalysts from burning. The PdCu/C catalysts were then treated at 260 °C under O_2 for 1 h to remove the remaining high boiling point capping agent. Then, the catalysts were treated under a H_2 atmosphere at different temperatures ranging from 30 to 800 °C. The samples are denoted as PdCu/C (H_2/T), where "H_2/T" represents the thermal treatment temperature under H_2. The absence of this label means O_2 treatment without H_2 treatment. Note that during the process of O_2 treatment, the O_2 concentration varied as 0%, 10%, and 20% O_2, balanced by N_2 at a specific flow rate of 150 mL/min. Flow rates of 20, 50, 100, and 150 mL/min at a constant O_2 concentration of 20% were also investigated in this work.

Physical Characterization. The chemical composition of PdCu/C NPs was analyzed by inductively coupled plasma−optical emission spectroscopy (ICP-OES) using a PerkinElmer 2000 DV ICP-OES instrument.[36] A Hitachi H-7000 electron microscope and JEM-2200FS instrument were employed to carry out transmission electron microscopy (TEM) and high-resolution transmission electron microscopy (HRTEM), respectively. A FEI Talos F200X microscope, used to characterize the morphology of the NPs in scanning transmission electron microscopy (STEM) mode, is equipped for energy-dispersive X-ray spectroscopy (EDS) (Super X) for precise and fast mapping. A Phillips X'pert PW 3040 MPD diffractometer was used to collect X-ray diffraction (XRD) data from 15° to 90° 2θ with a step size of 0.033° at room temperature. Cu Kα radiation (λ = 1.5418 Å) and a sealed Xe proportional detector were used. High-energy X-ray diffraction (HE-XRD) experiments were carried out using Ag Kα radiation (λ = 0.559 Å) with higher energy to collect XRD data from 13° to 90° 2θ with a step size of 0.05° at room temperature. HE-XRD data were reduced to atomic pair distribution functions (PDFs) $G(r)$. A Physical Electronics Quantum 2000 scanning ESCA microprobe was used to conduct X-ray photoelectron spectroscopy (XPS) experiments. An excitation source of focused monochromatic Al Kα X-ray (1486.7 eV), a 16-element multichannel detection system, and a spherical section analyzer were assembled on the instrument. A 100 μm diameter X-ray beam was rastered over a 0.2 × 1.4 mm rectangular spot on the sample. The binding energy (BE) was calibrated by the C 1s peak at 284.6 eV. The mass metal loading of the catalysts was determined by thermogravimetric

DOI: 10.1021/acscatal.8b03106
ACS Catal. 2018, 8, 11302−11313

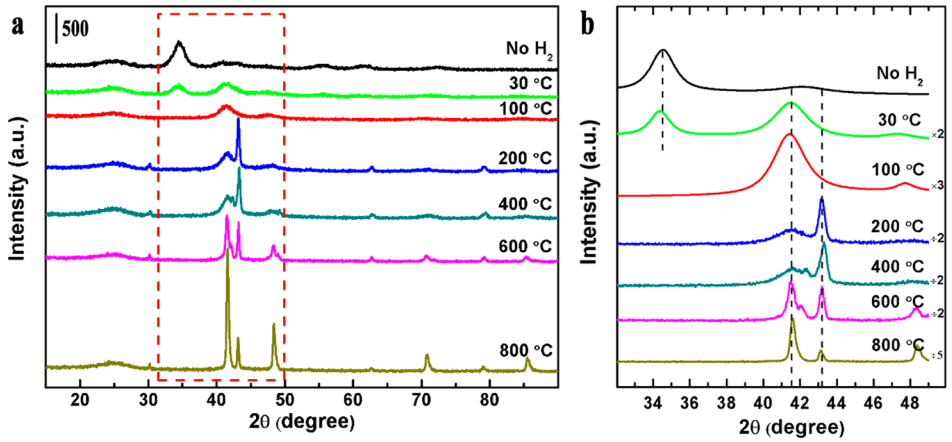

Figure 2. (a) XRD patterns for samples of PdCu/C catalysts as a function of H_2 thermal treatment conditions. (b) A magnified view of the boxed region in panel a for a better visual comparison.

analysis (TGA) conducted on a PerkinElmer Pyris 1-TGA instrument. The exact weight loadings of the PdCu/C catalysts studied here were within 23−25% and are shown in Table S1 of the Supporting Information (SI).

Electrochemical Measurement. Glassy carbon (GC) disks (geometric area 0.196 cm^2) were polished by 1 μm and then 0.05 μm Al_2O_3 powders. The catalyst inks were prepared by suspending 10 mg of PdCu/C NPs catalysts in 5 mL of deionized aqueous solution containing Nafion and 2-propanol (4.5:0.05:0.45, v/v/v), followed by ultrasonicating for 30 min to achieve a well-suspended solution. The polished GC was then coated with 15 μL of homogeneous ink and dried under room temperature for 1 h to be used as the working electrode. The cyclic voltammetry (CV) and rotating disk electrode (RDE) measurements were implemented by an electrochemical analyzer (CHI620a, CH Instruments) in a three-electrode cell at 23−24 °C. Before CV, the solution (0.1 M $HClO_4$) was deaerated with high-purity nitrogen. Afterward, the solution was saturated with oxygen for RDE measurements. A coiled Pt wire electrode (with a large surface area) was used as the counter electrode and a reversible hydrogen electrode (RHE) filled with 0.1 M $HClO_4$ was used as the reference electrode.

Computational Details. Periodic DFT calculations were carried out using the DMol[3] package in the Materials Studio software. The Perdew−Burke−Ernzerhof (PBE) functional with a generalized gradient approximation (GGA) was used to describe the exchange−correlation interaction. The spin unrestricted DFT calculations were performed, and a double-numerical basis set with polarization functions (DNP) was used. Two types of crystal structural bulks, i.e., fcc and bcc, were used to create the surface models. The (111) and (100) facets of fcc structure and the (110) and (100) facets of bcc structure were used to study the O_2 cleavage reaction.[37,38] A (5 × 5 × 1) k-point mesh was carried out to sample the surface Brillouin zone. A 15 Å vacuum along the z-direction was used between the repeated slabs. The adsorption species described were fully relaxed, and $\Delta E_{ad} = E_{adsorbate} + E_{metal\ surface} - E_{adsorbate/metal\ surface}$ was used to calculate the adsorption energies of adsorbates on each surface, where $E_{adsorbate}$, $E_{metal\ surface}$, and $E_{adsorbate/metal\ surface}$ are the total energy for the isolated adsorbate molecule, the isolated metal surface model, and the adsorbate adsorption on metal surfaces, respectively. The transition states on each model were located and optimized for an O_2 cleavage reaction, with only one imaginary frequency. The barrier of the reaction was calculated by $\Delta E_a = E_{TS} - E_{IS}$, where the energies of the transition state (E_{TS}) and the reactant (E_{IS}) were obtained with ZPE corrections. The d-band centers of pure metal and alloy surfaces were also calculated for the surface layer atoms.

3. RESULTS AND DISCUSSION

Nanoparticle Composition and Morphology. The composition of as-synthesized PdCu NPs was determined by ICP-OES. The results were highly consistent with the feeding ratio of the two metal precursors (1:1). A representative set of HAADF-STEM and EDS mapping for PdCu/C (H_2/100 °C) catalyst provided detailed information on the elemental distribution of Pd and Cu, as seen in Figure 1a−c, which shows the uniform distribution of the bimetallic composition across the nanoalloy. The uniformity of the bimetallic composition distribution was further confirmed for both small and large size particles after thermochemical processing over PdCu/C (H_2/100 °C) catalyst, as shown in Figure 1d−f. A representative set of TEM and HRTEM images for as-synthesized PdCu NPs are shown in Figure 1g,h. The average size of the as-synthesized PdCu NPs was 4.2 ± 0.4 nm. As shown by the HR-TEM image in Figure 1h, the lattice fringe of 0.217 nm is characteristic of the (111) plane of the fcc structure. An EDS spectrum was collected which showed the presence of Pd and Cu elements, as shown in Figure 1i.

As shown in Figure S1 (SI), the particle size of PdCu/C without thermal treatment under H_2 showed a slight increase to 5.1 ± 0.5 nm. For the PdCu/C (H_2/100 °C) catalyst, as shown in Figure S1a (SI), the average particle size decreased slightly to 4.6 ± 0.5 nm and the PdCu NPs exhibited a very uniform distribution on the carbon support. The average particle sizes of the PdCu NPs showed 5.7 ± 1.1, 7.6 ± 2.2, 13.8 ± 3.8, and 52.7 ± 18.8 nm for H_2 treatments at 200, 400, 600, and 800 °C, respectively, exhibiting a certain degree of sintering for thermal treatment at elevated temperatures under H_2.

Phase and Structural Properties. The phase structures of the nanocatalysts were analyzed by both in-house XRD and HE-XRD characterizations. Figure 2 shows in-house powder XRD patterns for PdCu/C catalysts treated at different temperatures under H_2. The peaks at 41.5°, 48.4°, and 71.0° correspond to 111, 200, and 220 atomic planes of the fcc

DOI: 10.1021/acscatal.8b03106
ACS Catal. 2018, 8, 11302−11313

structure, respectively. The peaks at 30.0° and 43.2° correspond to 100 and 110 atomic planes of the bcc structure, respectively.[39] In Figure 2, a single broad diffraction peak characteristic of CuO oxide phase is observed for the sample without H_2 treatment, indicative of oxidation under O_2 thermal treatment. After H_2 thermal treatment at 30 °C, the oxide was partially reduced and a peak of 111 Bragg peak of an fcc alloy emerged. At 100 °C, the NPs were fully reduced and a single, broad peak characteristic to fcc alloy appeared. The treatments at 200 and 400 °C under H_2 led to the phase separation in the NPs. The bcc structure emerged when the H_2 thermal treatment temperature was equal to or greater than 200 °C. The fcc and the bcc structures appeared to coexist in a broad temperature range (200−800 °C). At 600 °C, the fcc peaks become very sharp, indicative of a particle size increase. The XRD patterns of samples treated under different O_2 concentrations and flow rates were also measured (see Figure S2, SI), showing subtle difference in both fcc and bcc peaks.

Detailed phase structures of the nanocatalysts were revealed by analyzing the atomic PDFs extracted from HE-XRD patterns (see Figure S3, SI). The PdCu/C (H_2/400 °C) catalyst was first examined using HE-XRD/PDF, which revealed a clear phase segregation (Figure S3a, SI) consistent with our early findings.[32] We systematically examined the phase structures of the catalyst treated at different temperatures. The PDF results in Figure 3 show that the phase states

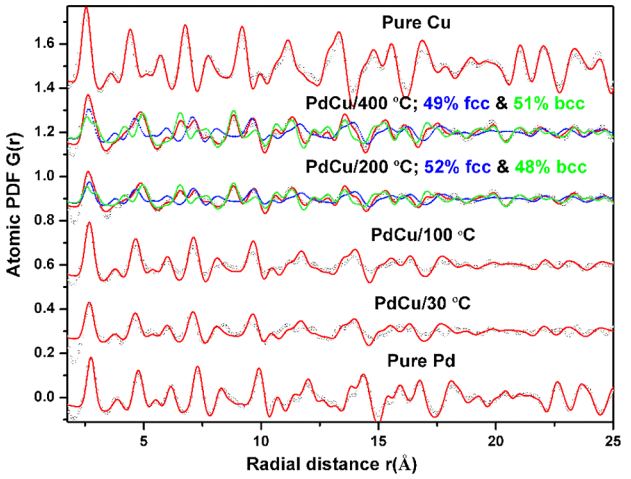

Figure 3. Experimental (symbols) and crystal structure model-derived (lines) atomic PDFs for PdCu/C H_2 thermally treated under different temperatures varying as 30, 100, 200, and 400 °C, along with PDFs for pure Pd and Cu. Red lines represent the best fit of the respective model to the experimental data. Note that blue lines represent the contribution of the fcc structure and green lines denote the bcc structure of the PdCu alloys processed at 200 and 400 °C. The corresponding lattice parameters of pure Cu, pure Pd, PdCu/C (H_2/30 °C), and PdCu/C (H_2/100 °C) are 3.626, 3.902, 3.803, and 3.812 Å, respectively. Lattice parameters of fcc and bcc phases for PdCu/C (H_2/200 °C) are 3.808 and 2.972 Å, respectively. Lattice parameters of fcc and bcc phases for PdCu/C (H_2/400 °C) are 3.791 and 2.973 Å, respectively.

of PdCu/C catalysts strongly depend on the H_2 thermal treatment temperatures. PdCu/C (H_2/30 °C) and PdCu/C (H_2/100 °C) catalysts feature single-phase alloys with chemically disordered fcc structure. Note that HE-XRD has a deeper penetration depth than regular XRD. However, HE-XRD/PDF examination of PdCu/C (H_2/30 °C) revealed no oxide species. Moreover, PdCu/C (H_2/200 °C) and PdCu/C (H_2/400 °C) showed phase segregation into a mixture of chemically disordered fcc and chemically ordered bcc structures, with 52% fcc and 48% bcc for the PdCu/C (H_2/200 °C) catalyst. The percentage of fcc structure decreased slightly to 49% when the temperature was raised to 400 °C. A fcc-type lattice parameter of 3.812 Å was obtained from the data of the PdCu/C (H_2/100 °C) catalyst.

The nanocatalysts were further examined by XPS analysis to determine the electronic structures of the catalysts and the valence states of the surface metals. Figure 4a shows a set of XPS spectra in the Cu 2p region for PdCu/C NPs treated at different temperatures under H_2. The two doublet features correspond to Cu^0 (932.0 eV $2p_{3/2}$ and 951.8 eV $2p_{1/2}$) and Cu^{2+} (934.2 eV $2p_{3/2}$ and 954.2 eV $2p_{1/2}$) chemical states. Similarly, the Pd 3d spectra containing the Pd $3d_{5/2}$ and Pd $3d_{3/2}$ states also exhibit two doublets, corresponding to Pd^0 (335.4 eV $3d_{5/2}$ and 340.8 eV $3d_{3/2}$) and Pd^{2+} (336.5 eV $3d_{5/2}$ and 342.0 eV $3d_{3/2}$) chemical states,[19,21] respectively, as shown in Figure 4b. The deconvoluted XPS peak positions are shown in Table S2 (SI). The majority of the Cu and Pd atoms in PdCu/C NPs after annealing (from 100 to 800 °C) under H_2 are in the metallic state. The peak intensity for Cu^{2+} and Pd^{2+} weakens significantly for PdCu/C (H_2/600 °C) and PdCu/C (H_2/800 °C), indicating that the surface metallic oxide was mostly reduced. However, the Cu^0 and Pd^0 peaks disappeared and the Cu^{2+} and Pd^{2+} states are dominant characteristics for PdCu/C without H_2 treatment, as shown in Figure 4a,b, meaning that the surface metals stayed mostly in the oxidized state. The ratios of Cu/Cu^{2+} and Pd/Pd^{2+} species in PdCu nanoalloys are shown in Table S3 (SI). It was found that the relative ratio of Cu^0 to Cu^{2+} increases gradually from 0.70 to 1.42 as the H_2 thermal treatment temperature increases from 100 to 800 °C. The relative ratio of Pd^0 to Pd^{2+} also increases gradually as the annealing temperature increases, showing a predominant Pd^0 state when the annealing temperature is higher than 600 °C. The size change of the NPs is believed to play an important role in this observation. The ratio of surface atoms to atoms in the core for smaller NPs is greater than that of larger-sized NPs. NPs with smaller sizes are oxidized more easily than bigger ones, since they have a higher specific surface area. Note that the samples were exposed to air before XPS experiments, so the surfaces were oxidized to a certain degree to Cu^{2+} and Pd^{2+} states. In terms of binding energy shifts, there is a subtle difference among PdCu/C catalysts annealed in H_2 under different temperatures. The position of the binding energy of Cu^0 $2p_{3/2}$ was slightly positively shifted for PdCu/C catalysts treated at temperatures lower than 800 °C under H_2 compared to that of PdCu/C (H_2/800 °C), suggesting the appearance of partial positive charges on Cu. This likely reflects the charge transfer from Cu to Pd due to the difference in electronegativity between Pd (2.2) and Cu (1.9).

The relative surface compositions of PdCu/C catalysts were also analyzed (Figure S4, SI). The surface composition percentage of Pd decreased slightly with increasing H_2 treatment temperature. These results reflected a subtle difference in terms of the relative surface enrichment on the catalysts.

Electrocatalytic Properties for the Oxygen Reduction Reaction. The ORR over PdCu/C catalysts treated at different thermochemical treatment conditions were studied to assess the electrocatalytic activity. Three different sets of thermal treatment conditions were investigated, including the

DOI: 10.1021/acscatal.8b03106
ACS Catal. 2018, 8, 11302−11313

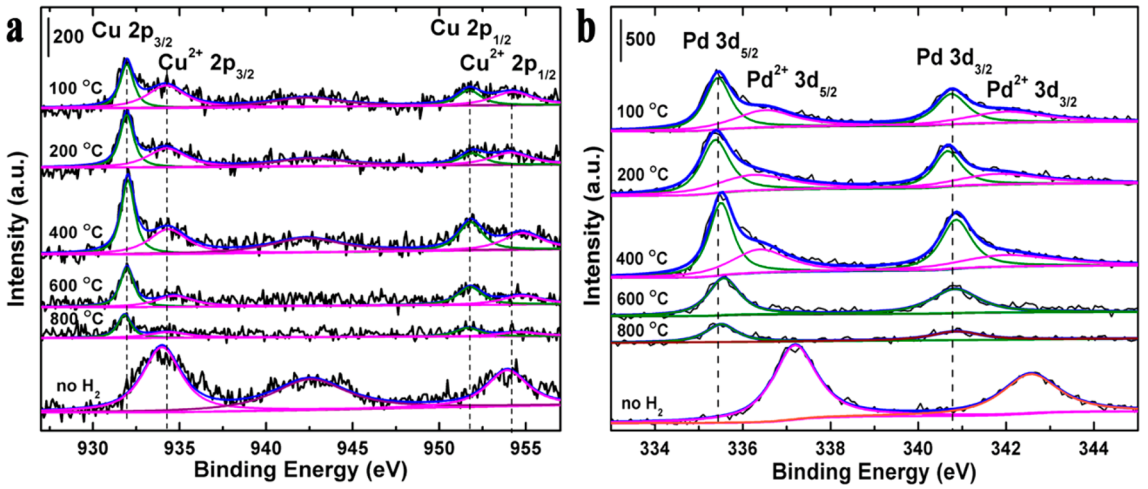

Figure 4. XPS spectra and deconvoluted peaks for PdCu/C NPs thermally treated with H_2 at different temperatures in regions of (a) Cu 2p and (b) Pd 3d.

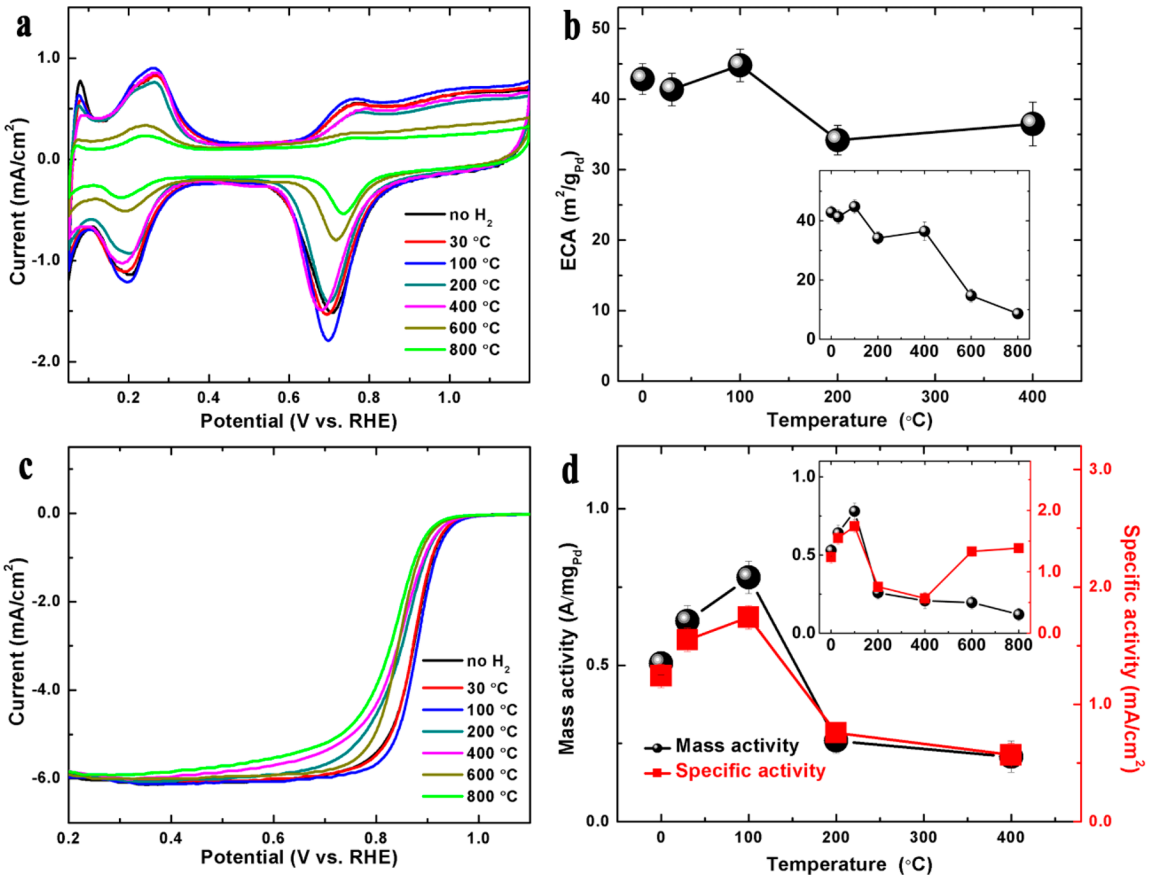

Figure 5. Electrochemical and electrocatalytic characteristics of PdCu/C catalysts thermally treated at different H_2 temperatures. (a) CV curves. (b) ECSA values vs annealing temperature. Inset: inclusion of the data points for the higher annealing temperatures (600−800 °C). (c) RDE curves. (d) MA and SA data at 0.850 V (vs RHE) vs annealing temperature. Inset: inclusion of the data points for the higher annealing temperatures (600−800 °C). Electrode, glassy carbon (geometric area 0.196 cm^2) coated with 15 μL of catalyst ink; electrolyte, 0.1 M $HClO_4$ saturated with high-purity N_2 for CV and saturated with high-purity O_2 for RDE; scan rate, 50 mV/s for CV and 10 mV/s for RDE; rotation speed for RDE, 1600 rpm.

H_2 treatment temperature, the O_2 concentration, and the flow rate. The CV and the RDE data were collected to access the electrocatalytic performance of the ORR in terms of the electrochemical active surface area (ECSA), mass activity (MA), and specific activity (SA).

A representative set of CV curves for PdCu/C catalysts treated at different temperatures under H_2 is shown in Figure 5a, revealing clear differences between different samples. The voltammetric peak characteristics in the hydrogen adsorption and desorption regions (0.135−0.400 V) were used to determine ECSA (Figure 5b). The PdCu/C (H_2/30 °C)

DOI: 10.1021/acscatal.8b03106
ACS Catal. 2018, 8, 11302−11313

catalyst showed an ECSA value of 41.4 m^2/g_{Pd}. A maximum ECSA value of 44.8 m^2/g_{Pd} was observed on the PdCu/C (H_2/100 °C) catalyst. The ECSA decreased upon further increasing the annealing temperature under H_2; an especially sharp ECSA drop was shown on catalysts thermally annealed under H_2 at temperatures which are higher than 400 °C, reflecting mostly the particle size increase. Note that PdCu/C without H_2 treatment still showed an ECSA of 42.8 m^2/g_{Pd}. This is attributed to the electrochemical reduction of the oxidized species on the NPs, a detailed study of which is part of our ongoing work. The ECSA was also examined by CO stripping measurements (Figure S5, SI) for validation. On the basis of the CO stripping results, a ratio of 1.0:1.1 was found for $ECSA_H$:$ECSA_{CO}$, which is consistent with those reported in the literature.[40] Therefore, these findings demonstrated that the ECSA values determined by the hydrogen adsorption peaks from the cyclic voltammetric measurements were very similar to those from the CO stripping measurements.

The RDE measurements for different temperatures of H_2-treated catalysts were performed in O_2-saturated 0.1 M $HClO_4$ electrolyte to obtain the kinetic currents, as revealed in Figure 5c. The mass activity and specific activity data as a function of thermal treatment temperature are shown in Figure 5d based on the kinetic currents read at 0.850 V (vs RHE). As shown in Figure 5c,d, the PdCu/C (H_2/30 °C) catalyst showed a mass activity of 0.64 A/mg_{Pd}, which is attributed to the insufficient calcination at low temperatures in a H_2 atmosphere.

The PdCu/C (H_2/100 °C) catalyst was found to exhibit the highest mass activity (0.78 A/mg_{Pd}) for the ORR, which is almost 8 times higher than that of the commercial Pd/C catalyst (see Table S1 and Figure S6, SI). This unprecedented low annealing temperature (100 °C) while yielding extremely high activity was first demonstrated in this paper. This catalyst has a pure fcc structure and shows considerably high catalytic activity for the ORR. The PdCu/C (H_2/200 °C) catalyst features a mixture of fcc and bcc structures, which exhibits a much lower catalytic activity than that for PdCu/C (H_2/100 °C) catalyst. The mass activity is shown to drop significantly with the increase in H_2 treatment temperature. Details of the correlation between the catalytic activity and the phase structure will be discussed in the next section. PdCu/C without H_2 treatment revealed a medium mass activity of 0.53 A/mg_{Pd}, suggesting that the electrochemical activation process plays a crucial role in the catalytic activity, an in-depth understanding of which is part of our future work. In general, PdCu/C catalyst with an fcc structure shows a higher catalytic activity than catalyst with a mixture of fcc and bcc structures. Similar trends were shown for the MA and SA values extracted at 0.900 V (vs RHE), as shown in Figure S7 (SI). The stabilities of the catalysts with fcc structure (100 °C) and those with a mixture of fcc and bcc structures (400 °C) were also examined (Figure S8, SI) in an accelerated durability test. While the catalyst with fcc structure showed a clear decay of stability, the mass activity was still much higher than for those with the mixed phase structures after the durability test.

We also examined the impact of O_2 concentration during the thermal treatment, a key step in removing the organic capping materials on the NPs,[30] on the catalyst's catalytic activity. A slight increase of MA was observed for catalysts treated under an increased O_2 concentration (Figure S9, SI). However, we point out here that a higher concentration of O_2 (>20% O_2) could cause severe burning of the carbon support, thus leading to severe particle aggregation. Hence, to prevent the catalyst from burning while effectively removing the capping agent, 20% O_2 for the thermal treatment was found to be an optimal balance. We also investigated the effect of O_2 flow rate on the catalyst's catalytic activity (Figure S10, SI). The mass activity strongly depends on the flow rates of O_2, showing a maximum catalytic activity for catalysts treated under an O_2 flow rate of 50 mL/min (0.21 A/mg_{Pd}). A higher flow rate apparently favors the removal of the organic species, but an overheating or burning could also happen, which leads to particle aggregation. A flow rate of 50 mL/min was found to be the optimal balance. Note that the RDE measurements were repeated for every sample, showing repeatable limiting currents. The measurements were also performed at different rotation speeds (Figure S11, SI), ensuring the accurate determination of the kinetic currents.

Structure−Activity Correlation. To aid the understanding of the correlation between the nanocrystal structure and the catalytic activity, DFT calculations of two types of PdCu crystal structures, i.e., fcc and bcc, were performed. Models with a Pd:Cu ratio of 1:1 in different crystal structures and different surfaces were built. We note here that the fcc-type model has a combination of Pd and Cu atoms on the surface. It is generally believed that the surface Cu is not stable under harsh acidic solution and may leach out during the initial potential scans. Indeed, the formation of a Pt/Pd skin upon leaching the base metals is currently the most often accepted viewpoint, which is largely based on a thermodynamic argument of bulk materials. However, recent findings of our in situ HE-XRD studies of Pt(Pd)M (M = base metals) catalysts suggested an alternative pathway for the remaining base metals in the nanoparticles, i.e., realloying, leading to a stable realloyed state in the nanoparticle and on the surface.[41] We therefore believe that the active sites of the nanoscale catalyst for ORR involved a combination of noble metals and base metals alloyed on the surface, in addition to those sites consisting of pure noble metal skin. It is the presence of alloyed surface sites that constitutes the basis for our computational modeling, while we do not rule out the possibility of active sites from a pure noble metal shell. Nevertheless, the surface activation and composition change did occur during potential cycling. On the basis of our previous study, PdCu catalyst with a composition of 50:50 could undergo about as much as 60% of Cu leaching out in acidic solution during the activation and electrochemical potential cycling processes.[18]

The calculation results are shown in Figures 6 and S12 (SI) and Table 1. The O_2 cleavage elementary reaction, a good descriptor of the ORR,[42] on an open surface plane (100) was studied first for both the fcc- and bcc-structured PdCu alloys. We considered the O−O cleavage reaction as a good descriptor of the activity for the ORR. While the rate-determining step was not assessed in this work, the results provided information for the fundamental understanding of the correlation between the phase structure and the catalytic activity. Considering that the removal of OH groups was reported previously as the rate-determining step for the ORR,[43,44] we examined the adsorption energies of OH species on PdCu alloy surfaces with different phase structures. As shown in Figure 6 and Table 1, the adsorption energy of O_2 on fcc-structured PdCu(100) surface (1.46 eV) is greater than that on bcc-structured PdCu(100) surface (1.32 eV). In terms of the O_2 cleavage step on fcc-structured (100) surface, a reaction barrier (0.21 eV) and a reaction energy (−1.24 eV)

DOI: 10.1021/acscatal.8b03106
ACS Catal. 2018, 8, 11302−11313

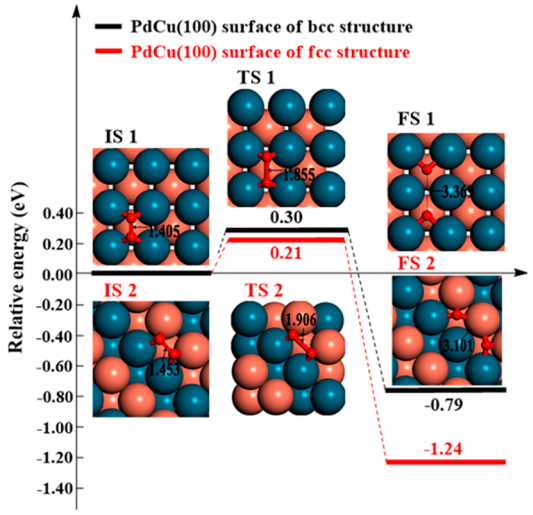

Figure 6. Energetics of the O−O bond cleavages of O_2 molecule on the PdCu(100) surface of bcc and fcc crystal structure. The key geometrical parameters are provided in angstroms. The big blue and coral balls are palladium and copper atoms, respectively; small red balls are O atoms.

were given. In comparison, a higher reaction barrier (0.30 eV) and a lower exothermic reaction energy (−0.79 eV) were obtained on bcc-structured PdCu(100). The product is more stable on the fcc-structured (100) surface. It is shown that the fcc-structured (100) has a higher catalytic activity for the O_2 bond-breaking step than the bcc-structured (100). The configurations of the reactants, transition states, and products are shown in Figure 6. The O−O bond distance in the reactant of fcc (100) surface model (IS2, 1.453 Å) is longer than that in the bcc (100) surface model (IS1, 1.405 Å). This phenomenon was also found in the configurations of the transition states, i.e., 1.906 Å (in TS2) > 1.855 Å in (TS1). The fcc-structured (100) surface stretches the O−O bond in O_2, favoring an easier cleavage of the O−O bond. The partial charge transfer on two O atoms in the reactant on the fcc (100) surface are −0.256 and −0.255 electrons, respectively, which are more negative than −0.232 and −0.231 electrons obtained on the bcc (100) surface (Table S4, SI). This finding indicates that the PdCu(100) surface with fcc structure can donate more electrons to the adsorbed O_2 molecule than the bcc-structured PdCu(100) surface, which favors breaking the O−O bond, leading to a more stable product. This theoretical finding is consistent with the experimental (XPS) finding that the charge on Cu is more positive than that on Pd. The rate constant of the forward reaction for O_2 cleavage on a fcc (100) surface is 6.4 times that on a bcc (100) surface, as shown in Table 1. In summary, the combination of O_2 adsorption energy, reaction barrier, product stability, configurations of reactants and transition states, charge distribution, and kinetics is suggestive of a higher catalytic activity for O_2 cleavage reaction on the fcc (100) surface than that on the bcc (100) surface.

The same elementary reaction, i.e., O−O bond cleavage in O_2, on close-packed PdCu alloy surfaces was also investigated, as shown in Table 1 (see also Figure S12, SI). In terms of fcc structure, PdCu(111) surface is the dominant facet. The adsorption energy of O_2 on PdCu(111) is 0.68 eV (weak chemisorption). The reaction barrier is 0.25 eV and the reaction energy is −1.24 eV, suggesting an extremely exothermic reaction. The O−O bond of O_2 is easy to break on the PdCu(111) surface but difficult to form, with a reverse reaction barrier of 1.45 eV. The reaction barrier on the (111) surface is higher than that of the (100) surface based on a fcc structure. The O−O bond distance in the transition state is 1.819 Å, which is 1.3 times higher than the O−O bond distance in the reactant (Figure S12, SI). This is consistent with the results reported previously, in which the bond distance in the transition state is 1.1−2.0 times the initial bond distance in the reactant.[45] In regard to the bcc structure, close-packed PdCu(110) surface is the most stable and dominant surface, which has been validated by the study done by Goddard's group.[34] In comparison with the PdCu(111) surface based on the fcc structure, a higher adsorption energy of 0.86 eV for O_2 species and a higher reaction barrier of 0.32 eV for the O_2 cleavage reaction were obtained on the PdCu(110) surface. The fcc alloy structure clearly has a higher catalytic activity for the O_2 cleavage reaction than the alloy with a bcc structure. This coincides with the results from the experiment where the PdCu/C (H_2/100 °C) catalyst with the pure fcc-type structure exhibited the highest catalytic activity for the ORR. For H_2 treatment at higher temperatures, a mixture of fcc and bcc structures was obtained, leading to lower catalytic performance. Moreover, fcc-structured (100) surface has higher catalytic activity for the O_2 cleavage reaction than both the fcc-structured (111) surface and the bcc-structured (100) surface.

Table 1 summarizes the results of the DFT calculation for the ORR on PdCu surfaces with different crystal structures. The adsorption energies of O_2 on the (100) surface of the fcc structure (1.46 eV) and on the (100) surface of the bcc structure (1.32 eV) are much higher than those on close-packed surfaces, i.e., 0.68 eV on the (111) surface of the fcc structure and 0.86 eV on the (110) surface of the bcc structure. Meanwhile, open surfaces also show a higher catalytic activity than close-packed surfaces. Those results suggest that stronger adsorption energies on open surfaces correspond to higher catalytic activities for ORR, while weaker adsorption energies on close-packed surfaces are related to lower activities. The activities of the catalysts could also be explained in terms of the valence electrons of the metals, especially the d-electrons.[26−28] The d-band center was calculated (see Table S5, SI). A higher

Table 1. Adsorption Energies of Reactant ($\Delta E_{ad,O_2}$), Reaction Barriers (ΔE_a), Reaction Energies (ΔE), Bond Distances in Reactant ($d_{O-O,R}$) and Transition State ($d_{O-O,TS}$), the Forward Reaction Rate Constants (k) at 373.15 K (100 °C), and the Only Imaginary Frequency (ν) on Each Type of Surface for the O_2 Cleavage Reaction

crystal structure	surface	Δ_{Ead,O_2} (eV)	ΔE_a (eV)	ΔE (eV)	$d_{O-O,R}$ (Å)	$d_{O-O,TS}$ (Å)	k (s^{-1})	ν (cm^{-1})
fcc	100	1.46	0.21	−1.24	1.453	1.906	2.34×10^{10}	302i
bcc	100	1.32	0.30	−0.79	1.405	1.855	3.67×10^{9}	332i
fcc	111	0.68	0.26	−1.19	1.436	1.819	3.82×10^{9}	424i
bcc	110	0.86	0.32	−1.31	1.434	1.897	1.27×10^{9}	391i

DOI: 10.1021/acscatal.8b03106
ACS Catal. 2018, 8, 11302−11313

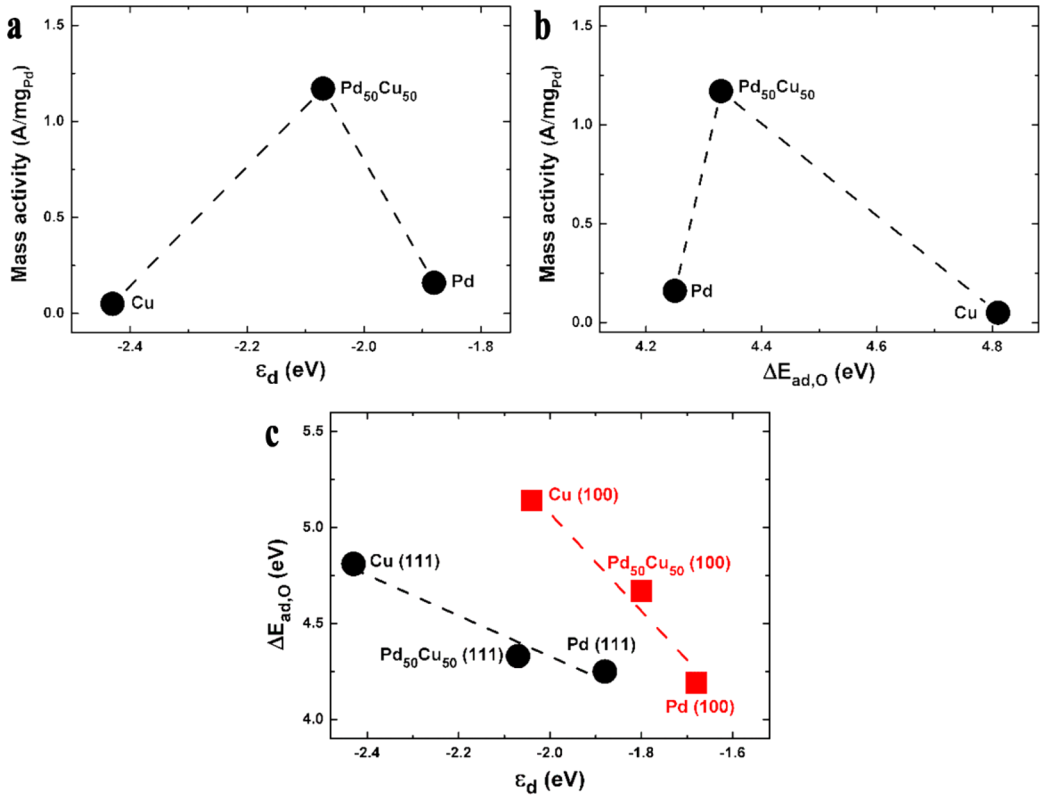

Figure 7. (a) Plot of the mass activities for ORR vs the d-band centers on (111) surfaces. (b) Plot of mass activities for ORR vs the adsorption energies of atomic oxygen on (111) surfaces. (MA data at 0.840 V). (c) Plot of adsorption energies of atomic oxygen vs the d-band centers on (111) and (100) surfaces.

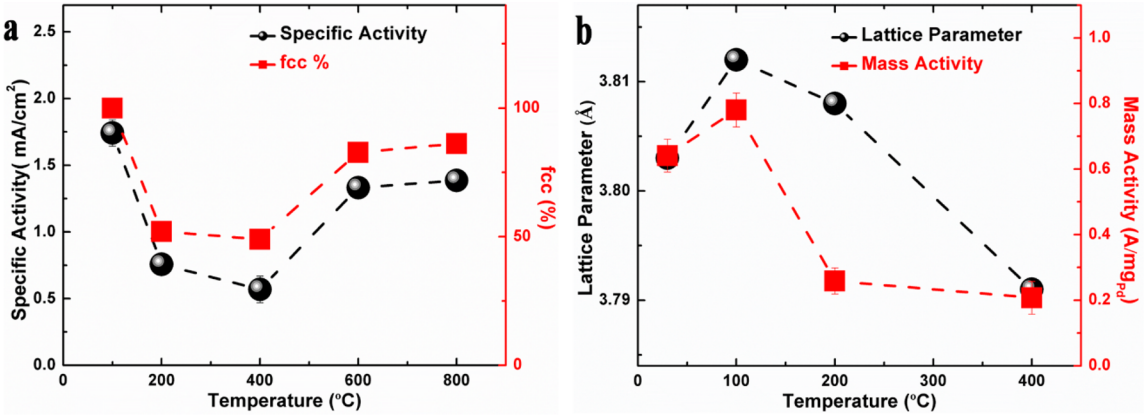

Figure 8. (a) Correlation between the specific activity (black circles) for the ORR and the percentage of fcc structure (red squares) in the PdCu/C catalysts annealed at different temperatures under H_2 atmosphere. (b) Correlation between the lattice parameters (black circles) of the fcc structure and the mass activities (red squares) for the ORR with PdCu/C catalysts annealed at different temperatures under H_2 atmosphere.

d-band center translates to stronger binding between the adsorbates and the metal.[27,46] In terms of the $Pd_{50}Cu_{50}$ alloy, a fcc-structured (111) surface reveals a lower d-band center (−2.07 eV) than that of a bcc-structured (110) surface (−1.68 eV). The lower energy d state is related to the Fermi level. The lower in energy the antibonding states are, the weaker the bond. The adsorption energy of atomic oxygen (4.33 eV) on the fcc-structured (111) surface is lower than that on the bcc-structured (110) surface (4.42 eV). The weakened adsorption of atomic oxygen on the fcc-structured catalyst in comparison with that of bcc-structured catalyst leads to a higher activity for the ORR. By examining the calculated chemisorption energies for OH on PdCu alloy surfaces with different phase structures (fcc/bcc) (see Table S6, SI), a weaker adsorption energy of OH species was found on PdCu alloy with a fcc structure in comparison with that on PdCu catalyst with a bcc structure. This finding suggests a higher activity for PdCu alloy with a fcc-type structure than that for PdCu alloy with a bcc-type structure. On each of these different phase structures, it was shown that a larger adsorption energy value was obtained for OH species on Cu−Cu bridge site than that on Pd−Pd bridge site. Upon protonation of the dissociated O species to form OH, the larger adsorption energy of OH on Cu sites would facilitate the migration of OH moiety from Pd to Cu sites, followed by further protonation to form a water molecule. Cu could thus play an important role in removing the intermediate

DOI: 10.1021/acscatal.8b03106
ACS Catal. 2018, 8, 11302−11313

OH species, but an assessment of the mechanistic details is part of our ongoing work.

The relationship between the mass activity and the d-band center for metals or alloys is depicted in Figure 7a. The addition of Cu into Pd to form the $Pd_{50}Cu_{50}$ alloy makes the d-band center of Pd negatively shift from −1.88 to −2.07 eV, which is also higher than that of Cu with −2.43 eV. The $Pd_{50}Cu_{50}$ alloy with the moderate d-band center reveals a significant enhancement of the catalytic activity compared to pure Pd or Cu. There is a clear synergy between Pd and Cu from the perspective of electronic properties. As shown in Figure 7b, the mass activity strongly depends on the adsorption energies of atomic oxygen on metal or alloy surfaces. Cu binds with O too strongly, making it difficult to desorb, thus poisoning the catalyst and reducing the activity. Pd binds O weakly. $Pd_{50}Cu_{50}$ alloy has moderate adsorption energy for the atomic oxygen, leading to the highest activity. On (111) or (100) surfaces, there is a good linear relationship between the adsorption energies of O and the d-band centers, as shown in Figure 7c. Furthermore, two different PdCu alloy lattice parameters, i.e., 3.802 and 3.812 Å, were used to calculate the reaction barriers of O−O bond breaking in O_2 on the (111) surface of the fcc structure. The results revealed negligible difference between the two different lattice parameters in terms of the reaction barriers.

From the above DFT results, it is concluded that PdCu alloys with an fcc structure exhibit a higher catalytic activity for the ORR than the bcc-structured catalyst. Open surfaces (100) revealed better activity than the close-packed (111) surface of the fcc structure and the (110) surface of the bcc structure. This finding has a significant implication for the design of fcc-structured PdCu alloy catalyst with open surfaces to achieve a higher catalytic activiy for ORR. Figure 8a shows the specific activity for the ORR and the percentage of fcc structure in the catalysts in correlation with the thermal treatment temperature. Overall, an excellent agreement was found for the specific activity and the percentage of fcc structure. PdCu/C (H_2/100 °C) catalyst features pure fcc and shows the highest specific activity. For the catalysts with a mixture of fcc and bcc structures obtained at 200−800 °C, the specific activity showed a drop before 400 °C and an increase after 400 °C. Both SA and the percentage of fcc decreased significantly for PdCu/C (H_2/200 °C) catalyst in comparison with those for PdCu/C (H_2/100 °C) catalyst. The minimal SA and percentage fcc were found for PdCu/C (H_2/400 °C) catalyst simultaneously. The percentage of fcc structure increased again to 83% and 86%, respectively, when the annealing temperature increased to 600 and 800 °C, at which point the particle sizes grew much bigger. For the bigger-sized NPs, the bcc structure transforms back to the fcc structure. The SA values showed an increase, which can be understood by taking the particle size effect into consideration. The particle size increased only slightly for treatments from 100 to 400 °C but increased greatly for treatments from 400 to 800 °C. The latter was reflected by the increase of SA. Therefore, the decrease of SA from 100 to 400 °C can be mainly attributed to the impact of the percentage of fcc structures on the activity. While the particle size also plays a role in the catalytic activity, the assessment of the activity using SA instead of MA took the particle size effect into consideration.[47,48] To further substantiate the findings, the synthesis of PdCu nanoalloy catalysts with pure bcc structure and similar particle sizes will be needed, which is part of our future work.

Figure 8b shows plots of the lattice parameter of the fcc structure and the mass activity in correlation with the thermal treatment temperature. The lattice parameters of the fcc structure were obtained from HE-XRD (Figure 3). A maximum lattice parameter of 3.812 Å was obtained for the PdCu/C (H_2/100 °C) catalyst. In terms of the H_2 annealing temperature, the lower (30 °C) or higher annealing temperature (200 or 400 °C) all lead to shrinkage of the lattice parameters. A maximum mass activity was also obtained at PdCu/C (H_2/100 °C). The lattice parameter is a crucial parameter in terms of its effect on the catalytic activities. The observation of the maximization of both the lattice parameter and the mass activity for the catalyst is intriguing, which is a subject of our future investigation.

4. CONCLUSION

Taken together, the results for the PdCu/C catalysts treated under controlled thermal treatment conditions have demonstrated the tunability of the nanocrystal alloy structures for ORR. The PdCu/C (H_2/100 °C) catalyst prepared by unprecedented low-temperature (100 °C) thermochemical treatment features a pure fcc structure and shows a higher catalytic activity for ORR than PdCu NPs featuring a mixture of fcc and bcc phases. The catalyst displays about 8 times greater mass activity than the commercial Pd/C catalyst. This activity is much higher than those of PdCu catalysts reported in the earlier work.[33] The fcc and bcc phase structures are shown to coexist over a broad temperature ranging from 200 to 800 °C under H_2 thermal treatment, which is substantiated by structural assessment based on HEXRD/PDFs analysis. While our conclusion was drawn largely by the catalysts treated at less than 200 °C that showed a similar particle size, we do recognize the increase of the particle size at higher temperatures, for which a further study of the relationship between catalytic activity and phase structure in terms of the particle size will be needed in our future investigations. Nevertheless, the finding that PdCu alloy catalysts with fcc structure have a higher catalytic activity for the ORR than those with bcc structure is further supported by DFT calculation, which aids the theoretical understanding of the experimental results. The results not only identified a new pathway to control the phase type of nanoalloy catalysts but also shined a new light onto the nanostructure−activity correlation at the atomic scale for the design, synthesis, and processing of highly active nanocatalysts.

■ ASSOCIATED CONTENT

Supporting Information

The Supporting Information is available free of charge on the ACS Publications website at DOI: 10.1021/acscatal.8b03106.

Additional experimental and theoretical data and additional characterization data, including TEM images, XRD, XPS, electrochemical tests, and DFT calculations (PDF)

■ AUTHOR INFORMATION

Corresponding Authors

*V.P. e-mail: petko1vg@cmich.edu.

*L.W. e-mail: lwang@chem.siu.edu.

*C.J.Z. e-mail: cjzhong@binghamton.edu.

ORCID

Valeri Petkov: 0000-0002-6392-7589

Lichang Wang: 0000-0002-6131-3532

DOI: 10.1021/acscatal.8b03106
ACS Catal. 2018, 8, 11302−11313

Chuan-Jian Zhong: 0000-0003-0746-250X

Present Address

[#]Z.-H.X.: Chemical Synthesis and Pollution Control Key Laboratory of Sichuan Province, College of Chemistry and Chemical Engineering, China West Normal University, Nanchong 637002, China

Notes

The authors declare no competing financial interest.

■ ACKNOWLEDGMENTS

This work was supported by the Department of Energy—Basic Energy Sciences (DE-SC0006877) and the National Science Foundation (CHE 1566283). Use of the Center for Nanoscale Materials, an Office of Science user facility, was supported by the U.S. Department of Energy, Office of Science, Office of Basic Energy Sciences (DE-AC02-06CH11357). The authors would like to thank Prof. David Jenkins of Binghamton University for his help in XRD measurements. Z.-P.W. also acknowledges the support of China Scholarship Council.

■ REFERENCES

(1) Gasteiger, H. A.; Markovic, N. M. Just a Dream—or Future Reality? *Science* **2009**, *324*, 48−49.
(2) Steele, B. C. H.; Heinzel, A. Materials for Fuel-Cell Technologies. *Nature* **2001**, *414*, 345−352.
(3) Shao, M.; Chang, Q.; Dodelet, J. P.; Chenitz, R. Recent Advances in Electrocatalysts for Oxygen Reduction Reaction. *Chem. Rev.* **2016**, *116*, 3594−3657.
(4) Srivastava, R.; Mani, P.; Hahn, N.; Strasser, P. Efficient Oxygen Reduction Fuel Cell Electrocatalysis on Voltammetrically Dealloyed Pt−Cu−Co Nanoparticles. *Angew. Chem., Int. Ed.* **2007**, *46*, 8988−8991.
(5) Stamenkovic, V. R.; Fowler, B.; Mun, B. S.; Wang, G.; Ross, P. N.; Lucas, C. A.; Markovic, N. M. Improved Oxygen Reduction Activity on $Pt_3Ni(111)$ via Increased Surface Site Availability. *Science* **2007**, *315*, 493−497.
(6) Greeley, J.; Stephens, I. E. L.; Bondarenko, A. S.; Johansson, T. P.; Hansen, H. A.; Jaramillo, F.; Rossmeisl, J.; Chorkendorff, I.; Nørskov, J. K. Alloys of Platinum and Early Transition Metals as Oxygen Reduction Electrocatalysts. *Nat. Chem.* **2009**, *1*, 552−556.
(7) Ji, X.; Lee, K. T.; Holden, R.; Zhang, L.; Zhang, J.; Botton, G. A.; Couillard, M.; Nazar, L. F. Nanocrystalline Intermetallics on Mesoporous Carbon for Direct Formic Acid Fuel Cell Anodes. *Nat. Chem.* **2010**, *2*, 286−293.
(8) Loukrakpam, R.; Wanjala, B. N.; Yin, J.; Fang, B.; Luo, J.; Shao, M.; Protsailo, L.; Kawamura, T.; Chen, Y.; Petkov, V.; Zhong, C. J. Structural and Electrocatalytic Properties of PtIrCo/C Catalysts for Oxygen Reduction Reaction. *ACS Catal.* **2011**, *1*, 562−572.
(9) Strasser, P. Catalysts by Platonic Design. *Science* **2015**, *349*, 379−380.
(10) Bu, L.; Zhang, N.; Guo, S.; Zhang, X.; Li, J.; Yao, J.; Wu, T.; Lu, G.; Ma, J. Y.; Su, D.; Huang, X. Q. Biaxially Strained PtPb/Pt Core/Shell Nanoplate Boosts Oxygen Reduction Catalysis. *Science* **2016**, *354*, 1410−1414.
(11) Li, M.; Zhao, Z.; Cheng, T.; Fortunelli, A.; Chen, C. Y.; Yu, R.; Zhang, Q.; Gu, L.; Merinov, B.; Lin, Z.; Zhu, E.; Yu, T.; Jia, Q.; Guo, J.; Zhang, L.; Goddard, W. A., III; Huang, Y.; Duan, X. Ultrafine Jagged Platinum Nanowires Enable Ultrahigh Mass Activity for the Oxygen Reduction Reaction. *Science* **2016**, *354*, 1414−1419.
(12) Shen, L. L.; Zhang, G. R.; Miao, S.; Liu, J.; Xu, B. Q. Core−Shell Nanostructured $Au@Ni_mPt_2$ Electrocatalysts with Enhanced Activity and Durability for Oxygen Reduction Reaction. *ACS Catal.* **2016**, *6*, 1680−1690.
(13) Feng, Y. Y.; Zhang, G. R.; Ma, J. H.; Liu, G.; Xu, B. Q. Carbon-Supported $Pt_\lambda Ag$ Nanostructures as Cathode Catalysts for Oxygen Reduction Reaction. *Phys. Chem. Chem. Phys.* **2011**, *13*, 3863−3872.
(14) Wang, X.; Kariuki, N.; Vaughey, J. T.; Goodpaster, J.; Kumar, R.; Myers, D. J. Bimetallic Pd−Cu Oxygen Reduction Electrocatalysts. *J. Electrochem. Soc.* **2008**, *155*, B602−B609.
(15) Lim, B.; Jiang, M.; Camargo, P. H. C.; Cho, E. C.; Tao, J.; Lu, X.; Zhu, Y.; Xia, Y. Pd-Pt Bimetallic Nanodendrites with High Activity for Oxygen Reduction. *Science* **2009**, *324*, 1302−1305.
(16) Zhang, L.; Hou, F.; Tan, Y. Shape-Tailoring of CuPd Nanocrystals for Enhancement of Electro-Catalytic Activity in Oxygen Reduction Reaction. *Chem. Commun.* **2012**, *48*, 7152−7154.
(17) Hu, G.; Nitze, F.; Gracia-Espino, E.; Ma, J.; Barzegar, H. R.; Sharifi, T.; Jia, X.; Shchukarev, A.; Lu, L.; Ma, C.; Yang, G.; Wågberg, T. Small Palladium Islands Embedded in Palladium−Tungsten Bimetallic Nanoparticles form Catalytic Hotspots for Oxygen Reduction. *Nat. Commun.* **2014**, *5*, 5253.
(18) Wu, J.; Shan, S.; Luo, J.; Joseph, P.; Petkov, V.; Zhong, C. J. PdCu Nanoalloy Electrocatalysts in Oxygen Reduction Reaction: Role of Composition and Phase State in Catalytic Synergy. *ACS Appl. Mater. Interfaces* **2015**, *7*, 25906−25913.
(19) Jiang, K.; Wang, P.; Guo, S.; Zhang, X.; Shen, X.; Lu, G.; Su, D.; Huang, X. Q. Ordered PdCu-Based Nanoparticles as Bifunctional Oxygen Reduction and Ethanol-Oxidation Electrocatalysts. *Angew. Chem., Int. Ed.* **2016**, *55*, 9030−9035.
(20) Chen, D.; Sun, P.; Liu, H.; Yang, J. Bimetallic Cu−Pd Alloy Multipods and their Highly Electrocatalytic Performance for Formic Acid Oxidation and Oxygen Reduction. *J. Mater. Chem. A* **2017**, *5*, 4421−4429.
(21) Cai, J.; Zeng, Y.; Guo, Y. Copper@Palladium-Copper Core-Shell Nanospheres as a Highly Effective Electrocatalyst for Ethanol Electro-Oxidation in Alkaline Media. *J. Power Sources* **2014**, *270*, 257−261.
(22) Xu, C.; Zhang, Y.; Wang, L.; Xu, L.; Bian, X.; Ma, H.; Ding, Y. Nanotubular Mesoporous PdCu Bimetallic Electrocatalysts toward Oxygen Reduction Reaction. *Chem. Mater.* **2009**, *21*, 3110−3116.
(23) Zhang, W.; Shan, S.; Luo, J.; Fisher, A.; Chen, J. F.; Zhong, C. J.; Zhu, J.; Cheng, D. Origin of Enhanced Activities for CO Oxidation and O_2 Reaction over Composition-Optimized $Pd_{50}Cu_{50}$ Nanoalloy Catalysts. *J. Phys. Chem. C* **2017**, *121*, 11010−11020.
(24) Kariuki, N. N.; Wang, X.; Mawdsley, J. P.; Ferrandon, M. S.; Niyogi, S. G.; Vaughey, J. T.; Myers, D. J. Colloidal Synthesis and Characterization of Carbon-Supported Pd-Cu Nanoparticle Oxygen Reduction Electrocatalysts. *Chem. Mater.* **2010**, *22*, 4144−4152.
(25) Tang, W.; Zhang, L.; Henkelman, G. Catalytic Activity of Pd/Cu Random Alloy Nanoparticles for Oxygen Reduction. *J. Phys. Chem. Lett.* **2011**, *2*, 1328−1331.
(26) Ruban, A.; Hammer, B.; Stoltze, P.; Skriver, H. L.; Nørskov, J. K. Surface Electronic Structure and Reactivity of Transition and Noble Metals. *J. Mol. Catal. A: Chem.* **1997**, *115*, 421−429.
(27) Hammer, B.; Nørskov, J. K. Theoretical Surface Science and Catalysis—Calculations and Concepts. *Adv. Catal.* **2000**, *45*, 71−129.
(28) Stamenkovic, V.; Mun, B. S.; Mayrhofer, K. J. J.; Ross, P. N.; Markovic, N. M.; Rossmeisl, J.; Greeley, J.; Nørskov, J. K. Changing the Activity of Electrocatalysts for Oxygen Reduction by Tuning the Surface Electronic Structure. *Angew. Chem.* **2006**, *118*, 2963−2967.
(29) Wanjala, B. N.; Loukrakpam, R.; Luo, J.; Njoki, P. N.; Mott, D.; Zhong, C. J.; Shao, M.; Protsailo, L.; Kawamura, T. Thermal Treatment of PtNiCo Electrocatalysts: Effects of Nanoscale Strain and Structure on the Activity and Stability for the Oxygen Reduction Reaction. *J. Phys. Chem. C* **2010**, *114*, 17580−17590.
(30) Wanjala, B. N.; Fang, B.; Loukrakpam, R.; Chen, Y.; Engelhard, M.; Luo, J.; Yin, J.; Yang, L.; Shan, S.; Zhong, C. J. Role of Metal Coordination Structures in Enhancement of Electrocatalytic Activity of Ternary Nanoalloys for Oxygen Reduction Reaction. *ACS Catal.* **2012**, *2*, 795−806.
(31) Wanjala, B. N.; Fang, B.; Shan, S.; Petkov, V.; Zhu, P.; Loukrakpam, R.; Chen, Y.; Luo, J.; Yin, J.; Yang, L.; Shao, M.; Zhong, C. J. Design of Ternary Nanoalloy Catalysts: Effect of Nanoscale Alloying and Structural Perfection on Electrocatalytic Enhancement. *Chem. Mater.* **2012**, *24*, 4283−4293.

DOI: 10.1021/acscatal.8b03106
ACS Catal. 2018, 8, 11302−11313

(32) Shan, S.; Petkov, V.; Prasai, B.; Wu, J.; Joseph, P.; Skeete, Z.; Kim, E.; Mott, D.; Malis, O.; Luo, J.; Zhong, C. J. Catalytic Activity of Bimetallic Catalysts Highly Sensitive to the Atomic Composition and Phase Structure at the Nanoscale. *Nanoscale* **2015**, *7*, 18936−18948.
(33) Wang, C.; Chen, D. P.; Sang, X.; Unocic, R. R.; Skrabalak, S. E. Size-Dependent Disorder-Order Transformation in the Synthesis of Monodisperse Intermetallic PdCu Nanocatalysts. *ACS Nano* **2016**, *10*, 6345−6353.
(34) Sha, Y.; Yu, T. H.; Merinov, B. V.; Goddard, W. A., III DFT Prediction of Oxygen Reduction Reaction on Palladium-Copper Alloy Surfaces. *ACS Catal.* **2014**, *4*, 1189−1197.
(35) Yang, L.; Shan, S.; Loukrakpam, R.; Petkov, V.; Ren, Y.; Wanjala, B. N.; Engelhard, M. H.; Luo, J.; Chen, Y.; Zhong, C. J.; Yin, J. Role of Support−Nanoalloy Interactions in the Atomic-Scale Structural and Chemical Ordering for Tuning Catalytic Sites. *J. Am. Chem. Soc.* **2012**, *134*, 15048−15060.
(36) Shan, S.; Petkov, V.; Yang, L.; Luo, J.; Joseph, P.; Mayzel, D.; Prasai, B.; Wang, L.; Engelhard, M.; Zhong, C. J. Atomic-Structural Synergy for Catalytic CO Oxidation over Palladium-Nickel Nanoalloys. *J. Am. Chem. Soc.* **2014**, *136*, 7140−7151.
(37) Błonski, P.; Kiejna, A. Structural, Electronic, and Magnetic Properties of bcc Iron Surfaces. *Surf. Sci.* **2007**, *601*, 123−133.
(38) Ferrin, P.; Kandoi, S.; Nilekar, A. U.; Mavrikakis, M. Hydrogen Adsorption, Absorption and Diffusion on and in Transition Metal Surfaces: A DFT Study. *Surf. Sci.* **2012**, *606*, 679−689.
(39) Marakatti, V. S.; Sarma, S. C.; Joseph, B.; Banerjee, D.; Peter, S. C. Synthetically Tuned Atomic Ordering in PdCu Nanoparticles with Enhanced Catalytic Activity toward Solvent-Free Benzylamine Oxidation. *ACS Appl. Mater. Interfaces* **2017**, *9*, 3602−3615.
(40) Shao, M.; Odell, J. H.; Choi, S.; Xia, Y. Electrochemical Surface Area Measurements of Platinum- and Palladium-Based Nanoparticles. *Electrochem. Commun.* **2013**, *31*, 46−48.
(41) Petkov, V.; Prasai, B.; Shan, S.; Ren, Y.; Wu, J.; Cronk, H.; Luo, J.; Zhong, C. J. Structural Dynamics and Activity of Nanocatalysts inside Fuel Cells by in Operando Atomic Pair Distribution Studies. *Nanoscale* **2016**, *8*, 10749−10767.
(42) Wang, L.; Williams, J. I.; Lin, T.; Zhong, C. J. Spontaneous Reduction of O_2 on PtVFe Nanocatalysts. *Catal. Today* **2011**, *165*, 150−159.
(43) Tripković, V.; Skúlason, E.; Siahrostami, S.; Nørskov, J. K.; Rossmeisl, J. The Oxygen Reduction Reaction Mechanism on Pt(1 1 1) from Density Functional Theory Calculations. *Electrochim. Acta* **2010**, *55*, 7975−7981.
(44) Duan, Z.; Wang, G. Comparison of Reaction Energetics for Oxygen Reduction Reactions on Pt(100), Pt(111), Pt/Ni(100), and Pt/Ni(111) Surfaces: A First-Principles Study. *J. Phys. Chem. C* **2013**, *117*, 6284−6292.
(45) Wu, Z.; Zhang, M.; Jiang, H.; Zhong, C. J.; Chen, Y.; Wang, L. Competitive C−C and C−H Bond Scission in the Ethanol Oxidation Reaction on Cu(100) and the Effect of an Alkaline Environment. *Phys. Chem. Chem. Phys.* **2017**, *19*, 15444−15453.
(46) Nørskov, J. K.; Abild-Pedersen, F. A.; Studt, F.; Bligaard, T. Density Functional Theory in Surface Chemistry and Catalysis. *Proc. Natl. Acad. Sci. U. S. A.* **2011**, *108*, 937−943.
(47) Koenigsmann, C.; Santulli, A. C.; Gong, K.; Vukmirovic, M. B.; Zhou, W.; Sutter, E.; Wong, S. S.; Adzic, R. R. Enhanced Electrocatalytic Performance of Processed, Ultrathin, Supported Pd−Pt Core−Shell Nanowire Catalysts for the Oxygen Reduction Reaction. *J. Am. Chem. Soc.* **2011**, *133*, 9783−9795.
(48) Koenigsmann, C.; Sutter, E.; Chiesa, T. A.; Adzic, R. R.; Wong, S. S. Highly Enhanced Electrocatalytic Oxygen Reduction Performance Observed in Bimetallic Palladium-Based Nanowires Prepared under Ambient, Surfactantless Conditions. *Nano Lett.* **2012**, *12*, 2013−2020.

DOI: 10.1021/acscatal.8b03106
ACS Catal. 2018, 8, 11302−11313